ADVANCED FUNCTIONAL MATERIALS
www.afm-journal.de



# Avalanche-Discharge-Induced Electrical Forming in Tantalum Oxide-Based Metal–Insulator–Metal Structures

*Katharina Skaja, Christoph Bäumer, Oliver Peters, Stephan Menzel, Marco Moors, Hongchu Du, Manuel Bornhöfft, Christoph Schmitz, Vitaliy Feyer, Chun-Lin Jia, Claus Michael Schneider, Joachim Mayer, Rainer Waser, and Regina Dittmann**

**Oxide-based metal–insulator–metal structures are of special interest for future resistive random-access memories. In such cells, redox processes on the nanoscale occur during resistive switching, which are initiated by the reversible movement of native donors, such as oxygen vacancies. The formation of these filaments is mainly attributed to an enhanced oxygen diffusion due to Joule heating in an electric field or due to electrical breakdown. Here, the development of a dendrite-like structure, which is induced by an avalanche discharge between the top electrode and the $Ta_2O_{5-x}$ layer, is presented, which occurs instead of a local breakdown between top and bottom electrode. The dendrite-like structure evolves primarily at structures with a pronounced interface adsorbate layer. Furthermore, local conductive atomic force microscopy reveals that the entire dendrite region becomes conductive. Via spectromicroscopy it is demonstrated that the subsequent switching is caused by a valence change between $Ta^{4+}$ and $Ta^{5+}$, which takes place over the entire former Pt/$Ta_2O_{5-x}$ interface of the dendrite-like structure.**

K. Skaja, C. Bäumer, O. Peters, Dr. S. Menzel, Dr. M. Moors, Dr. H. Du, M. Bornhöfft, C. Schmitz, Dr. V. Feyer, Prof. C.-L. Jia, Prof. C. M. Schneider, Prof. R. Waser, Prof. R. Dittmann
Peter Grünberg Institut
Forschungszentrum Jülich
52425 Jülich, Germany
E-mail: r.dittmann@fz-juelich.de

Dr. H. Du, M. Bornhöfft, Prof. C.-L. Jia, Prof. J. Mayer
Ernst Ruska-Centre for Microscopy and Spectroscopy with Electrons
Forschungszentrum Jülich
52425 Jülich, Germany

M. Bornhöfft, Prof. J. Mayer
Central Facility for Electron Microscopy
RWTH Aachen University
52056 Aachen, Germany

Prof. C. M. Schneider
Faculty of Physics
University of Duisburg
47048 Duisburg, Germany

Prof. R. Waser
Institute of Materials in Electrical Engineering and Information Technology II
RWTH Aachen University
52056 Aachen, Germany

**DOI: 10.1002/adfm.201502767**

## 1. Introduction

Resistive switching in transition metal oxides has attracted considerable attention as a candidate for nonvolatile memory in recent years, due to high scalability, fast switching speed, and low power consumption.[1–4] A large variety of binary metal oxides[5–7] and also complex transition metal oxides[8–11] was reported as possible candidates for memristive memories. Recently, significant progress has been made in the device performance for amorphous $Ta_2O_{5-x}$-based devices. High switching speed, long endurance (write cyclability), and low power consumption have been demonstrated.[12–14] A common model for the resistive switching in these materials is the valence change mechanism (VCM), where the movement of native donor dopants such as oxygen vacancies (or cation interstitials) leads to an enrichment or depletion of electrons in the conduction band. It is widely accepted that a nanoscale conductive filament is responsible for the resistance change in these cells. It is usually reported that the filament consists of an accumulation of mobile native donors with a typical width between 10 to 500 nm.[15–17] The voltage-driven movement of mobile donors and the associated electrochemical redox process in the conductive filament promote the switching between the low resistance state (LRS) and high resistance state (HRS).

Typically, a first quasi-static current–voltage ($I$–$V$) sweep with a voltage higher than the subsequent switching voltage is necessary to form this filament. At a certain voltage during the first sweep the current significantly increases and drives the change in the resistance of the cells. This process is called electroforming, which is commonly described as a self-accelerating process where increased conductivity and Joule heating mutually reinforce, leading to the formation of an oxygen deficient filament, which connects the bottom and top electrode.[4,11,18] It was observed that the filament preferentially nucleates at pre-existing defects of the metal–insulator–metal (MIM) structures.[19] For the first stage of electroforming in $Ta_2O_{5-x}$, a purely electronic mechanism has been reported, which is initiated by the applied electric field and results in reversible changes of the

device conductivity.[20] This first stage of forming was described as formation of a current path in the oxide layer, which takes place before ionic motion occurs in the oxide layer. As soon as Joule heating is sufficient for ionic movement, the formation of a filament starts as a consequence of oxygen vacancy movement, which results in a significantly decreased resistance within a filament region.

For $Ta_2O_{5-x}$-based MIM structures it has been previously demonstrated by Wei et al.[21] that $Ta_2O_{5-x}$ is reduced to $TaO_{2-x}$ during switching from HRS to LRS, but no spatially resolved data were provided in this work. Strachan and co-workers proved the formation of a single filament after electroforming by spatially resolved techniques, but could not detect differences between LRS and HRS.[22,23] Whereas most studies on $Ta_2O_{5-x}$-based MIM structures anticipate a filamentary switching process, some groups report on more spatially extended switching geometries. In particular, homogenous interface type switching was reported for $Ta_2O_{5-x}$ based cells.[24] Atomically resolved analysis of $Pt/Si/Ta_2O_{5-x}/TaO_{2-x}/Pt$ cells,[14] revealed multiple filaments which undergo a redox-process during resistive switching.

Therefore, the questions where redox-processes take place are still under controversial debate and its further elucidation is of key relevance.

In the current report, we will investigate the development of a conductive filament of a $Pt/Ta_2O_{5-x}/Ta$ cell during the electroforming process by performing a variety of complementary analysis techniques. In contrast to the common model of electroforming described above, we reveal that in the presence of a pronounced interface adsorbate layer (consisting of $H_2O$ and hydrocarbons), Joule heating or an electric breakdown in the oxide layer do not initiate the electroforming process. Instead, the presence of an adsorbate layer between the metal oxide and the top electrode enables an avalanche discharge at the interface, which leaves behind an oxygen deficient, conductive dendrite-like structure. These structures were investigated by scanning electron microscopy (SEM), nanoarea electron diffraction in scanning electron transmission microscopy (nanodiffraction in STEM) measurements, local conductive atomic force microscopy (LC-AFM), and photoelectron emission microscopy (PEEM). Spectromicroscopic measurements give an insight into the valence state of Ta for the low and high resistance state. We demonstrate that the remarkable differences between the low and high resistance state are caused by a valence change between $Ta^{5+}$ and $Ta^{4+}$ within the entire former $Pt/Ta_2O_{5-x}$ interface of the conductive area.

## 2. Results

$Ta_2O_{5-x}$-based MIM structures consisting of a $Pt/Ta_2O_{5-x}/Ta$ layer stack were electrically characterized by performing quasi-static current–voltage ($I$–$V$) sweeps. Details about the preparation of the samples are provided in the Experimental Section. Resistive switching in the as-prepared cells can be enabled by an initial electroforming step with positive or negative polarity at the top electrode. Afterward, the cells can be reversibly switched between LRS and HRS. As an example, a typical $I$–$V$ curve of the first and subsequent sweeps for positive forming is shown in **Figure 1**a. A positive voltage applied to the platinum top electrode enables the resistive switching and leads to

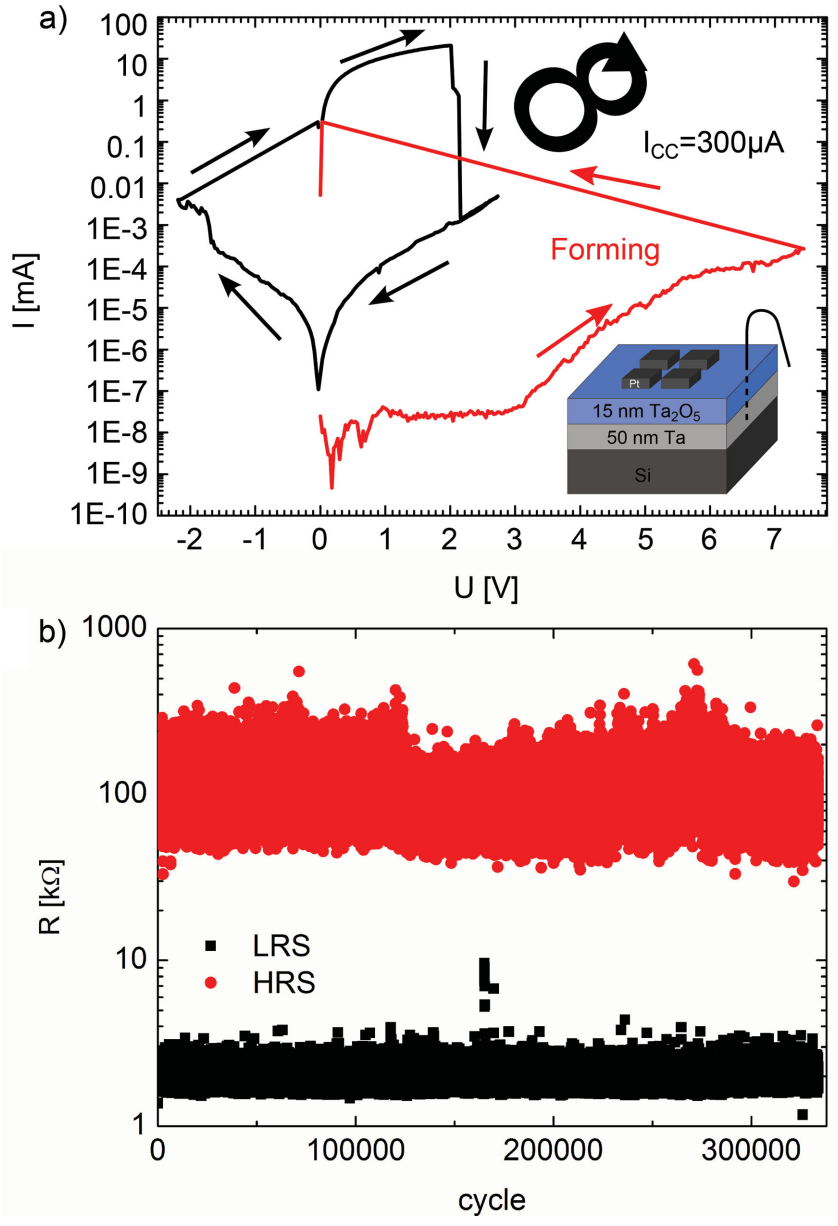


**Figure 1.** a) Quasi-static $I$–$V$ characteristic of a $Pt/Ta_2O_{5-x}/Ta$ device displayed by the black curve and an initial forming step (red curve). The voltage was applied to the top electrode. b) Endurance measurements of the structure with red dots as HRS and black dots as LRS.

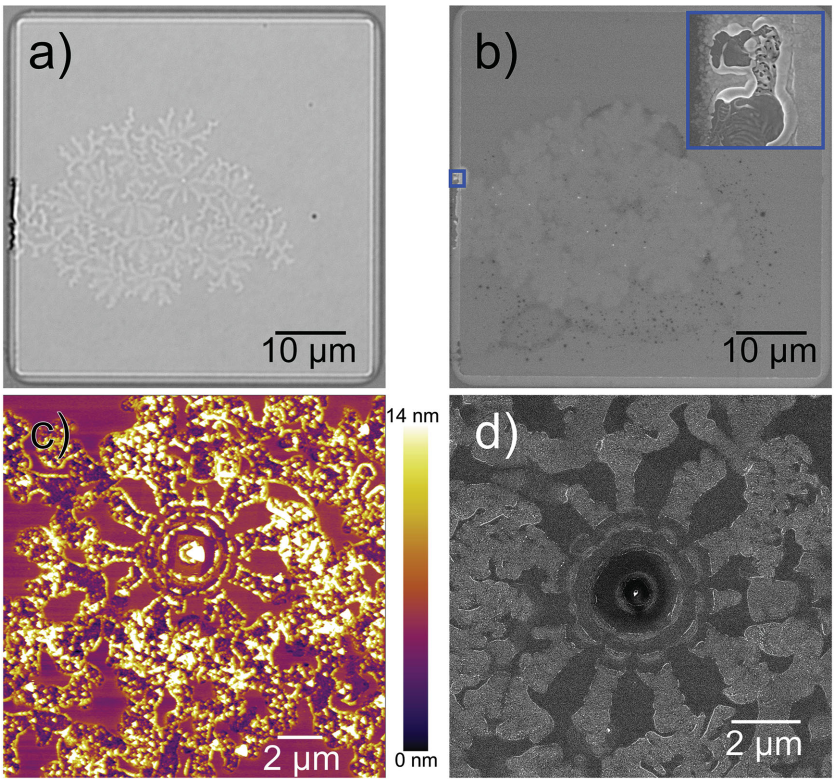


**Figure 2.** a) Optical microscope image of the nondelaminated Pt top electrode after electroforming. b) SEM image of the same electrode. The platinum electrode shows no peel off. Only at the left edge, the platinum seems to be melted due to Joule heating during the forming process. The inset in this picture shows a higher magnification image of a part of the left edge. c) AFM scan and d) SEM image of the dendrite-like structure after delamination.

a breakdown of the highly insulating initial state (>$10^{10}$ Ω) to the LRS (≈2 × $10^3$ Ω). After the initial forming step (+7.6 V), the cells can be switched in counter-eightwise polarity[25,26] and show an endurance of at least 3 × $10^5$ cycles (Figure 1b).

The switching characteristic and the endurance of cells formed with negative bias are similar to the cells formed with positive bias at the top electrode. However, only for the cells formed with a positive voltage morphological changes within the top electrode can be observed after electroforming. Therefore, only these devices are studied in more detail below. The morphological change of the top electrode after electroforming is shown in **Figure 2**a and resembles Lichtenberg figures,[27] which will be referred to as dendrite-like structures in the following. Despite morphological changes, the Pt electrode remains continuous, except for one edge, which appears to be melted due to Joule heating during the forming process (see Figure 2b).

After mechanical removal of the platinum top electrode (see the Experimental Section), we investigated the topography of the former Pt/$Ta_2O_{5-x}$ interface with AFM (Figure 2c). The dendrite-like structure is also observed in the $Ta_2O_{5-x}$ and can be clearly distinguished from the unaltered surrounding. Within this dendrite-like structure, there is a center with circular fronts of which dendrite-like "arms" extend to the outer regions. The dendrite-like structure has a grainy morphology, which is in some parts deeper than the unaltered surrounding area. In Figure 2d an SEM image of this dendrite-like structure is shown. The morphological change is also visible in the image. The dendrite-like structure appears brighter than the unaltered area, which might be caused by local variations of the work function, as will be discussed below.[28]

The structural changes in the dendrite-like region were investigated by STEM (for detail see the Supporting Information). The diffraction analysis (cf. Figure S1, Supporting Information) showed that no crystallization occurred within the dendrite structure.

In order to find out which parts of the cells with dendrite-like structures are conductive, we performed LC-AFM measurements with a tip bias of +10 V. This high voltage was necessary due to adsorbates on the surface of the $Ta_2O_{5-x}$ layer or a low conductivity of the cantilever. In the LC-AFM current scan (**Figure 3**a) we observe features with enhanced conductivity, which can be assigned to the dendrite-like structures (Figure 3b). The conductivity in the entire dendrite-like structure is increased and the unaltered surrounding is still insulating.

We thus demonstrated that during electroforming, a conductive, dendrite-like structure evolves inside an insulating matrix.

We anticipate that subsequent redox reactions, which are expected for each switching event, occur within these dendrite-like structures. To investigate switching-induced changes in the chemical composition or electrical properties, we analyzed cells in the LRS and HRS via energy filtered photoemission electron microscopy (PEEM). **Figure 4**a,b shows secondary electron PEEM images for a LRS and HRS cell, respectively. The dendrite-like region is visible for LRS and HRS in the

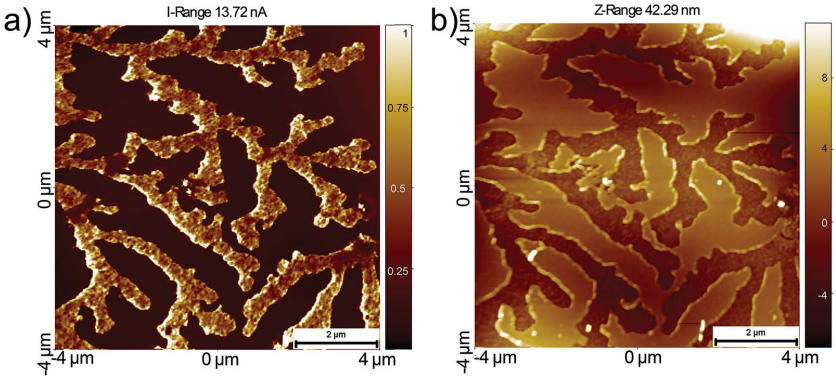


**Figure 3.** a) LC-AFM current scan of a part of the dendrite-like structure, probed at 10 V bias. b) The corresponding AFM scan. The dendrite-like structure shows an enhanced conductivity.

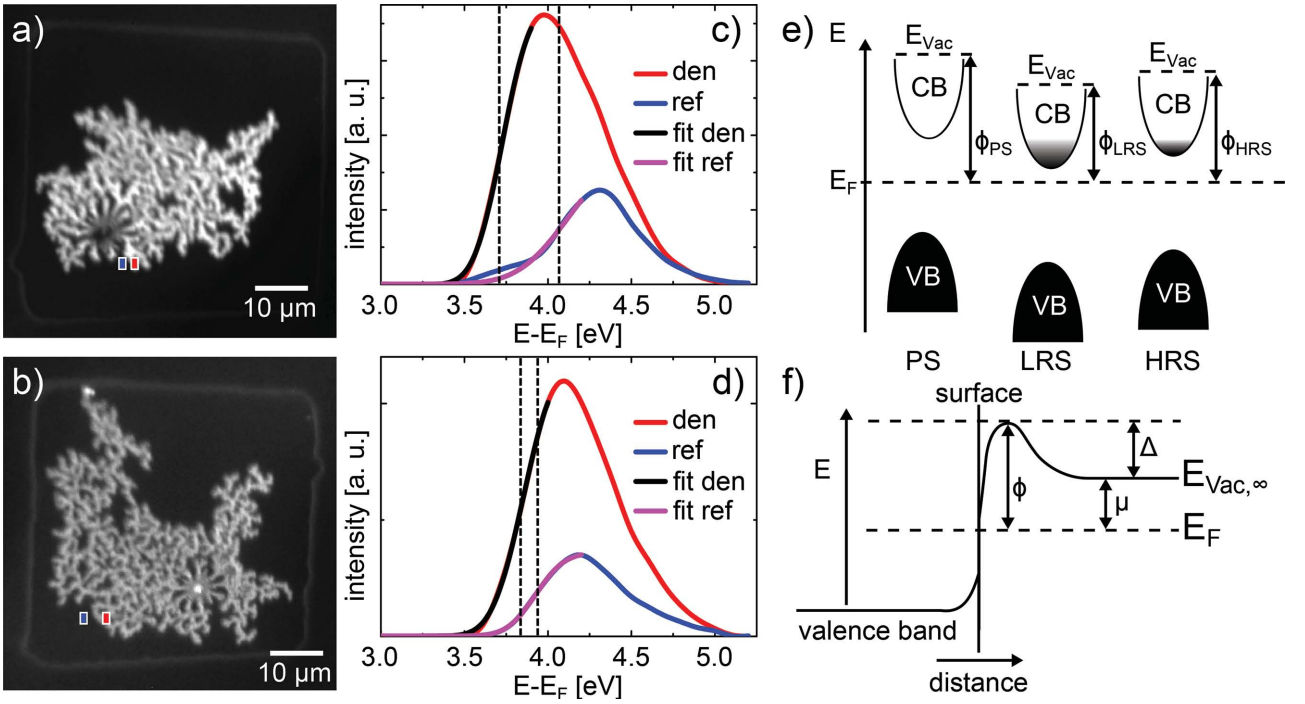


**Figure 4.** Work function images at a photon energy of 4 eV for an a) LRS and b) HRS cell and the extracted threshold photoemission spectra from regions of interest for the dendrite-like region (red rectangle) and a reference region (blue rectangle) for c) LRS and d) HRS. Depiction of a density of state diagram for the pristine state (PS), low resistance state (LRS), and high resistance state (HRS) demonstrate how the valence band (VB) and conduction band (CB) shifts in relation to the Fermi level ($E_F$) for different oxygen vacancy concentration (donors). e) In addition, the changes in work function are shown. f) Energy level diagram near a surface of a semiconductor illustrating that the work function ($\Phi$) is a composition of surface dipole ($\Delta$) and electrochemical potential ($\mu$).

work function contrast. For spectral information, PEEM image stacks with increasing electron energy were obtained for both cells and regions of interest (ROI) were defined. The spectral intensity was then extracted from each pixel within the ROI. The threshold photoemission spectra are shown in Figure 4c,d for LRS and HRS, respectively, where $E$–$E_F$ indicates the photoelectron energy above the Fermi level ($E_F$). The work function of the $Ta_2O_{5-x}$ layer can be determined from the secondary electron cut-off of the spectra and the energetic distance to the Fermi level. The work function values were extracted from the threshold spectra by fitting the emission threshold with a convolution of Gauss and Heaviside function.[29] Due to the strong influence of potential surface adsorbents on the work function,[30] only the relative changes between the dendrite-like region and unaltered surrounding will be considered instead of the absolute values.

Compared to the unaltered surrounding, the work function in the dendrite-like region is shifted toward lower energies for both LRS and HRS cells. The energy shifts are 0.4 eV and 0.1 eV for the LRS and HRS, respectively. As illustrated in Figure 4e, the increased work function can be explained by band bending of the conduction band toward the Fermi level.

This energy shift was also observed for oxygen deficient $Ta_2O_{5-x}$[31] and is consistent with an increase of the donor dopant concentration in a semiconductor.[32] The increased n-doping within this dendrite-like structure is consistent with the higher conductivity in comparison to the pristine state of the devices and confirm the LC-AFM measurements.

However, one has to keep in mind that the work function of a material does not only depend on the electrochemical potential (i.e., the band alignment), but also on the surface dipole (depicted in Figure 4f).[33] The electron chemical potential µ is defined as the position of the Fermi energy $E_F$ relative to the absolute vacuum level $E_{Vac,\infty}$ and the surface dipole Δ represents an additional energetic barrier to removing an electron from the solid's surface. This additional dipole barrier can be caused by electron density spilling from the solid surface[34] or by adsorbents at the surface. The crystallographic orientation,[29,35] surface roughness,[36] and adsorbents can influence the surface dipole.[30] However, the altered surface morphology could still be a reason for the work function shift due to surface dipoles. To unambiguously confirm that the work function shift corresponds to band bending and corresponding n-type doping, it must be shown that the core levels are also shifted.[37]

Therefore, spatially resolved Ta 4f core level scans were recorded for the LRS and HRS cells shown in Figure 4 by obtaining PEEM image stacks with increasing binding energy. In these image stacks (cf. Figure S2, Supporting Information) we observe a contrast between the dendrite-like regions and the unaltered surrounding area. These regions have a similar shape as the dendrite-like structure observed in the threshold images (cf. Figure 4a,b). To compare the photoemission spectra within the dendrite-like region and the unaltered surrounding, representative spectra were extracted for the dendrite-like and reference regions. The spectra are displayed in **Figure 5**a,b for LRS and HRS, respectively. Consistent with the observation

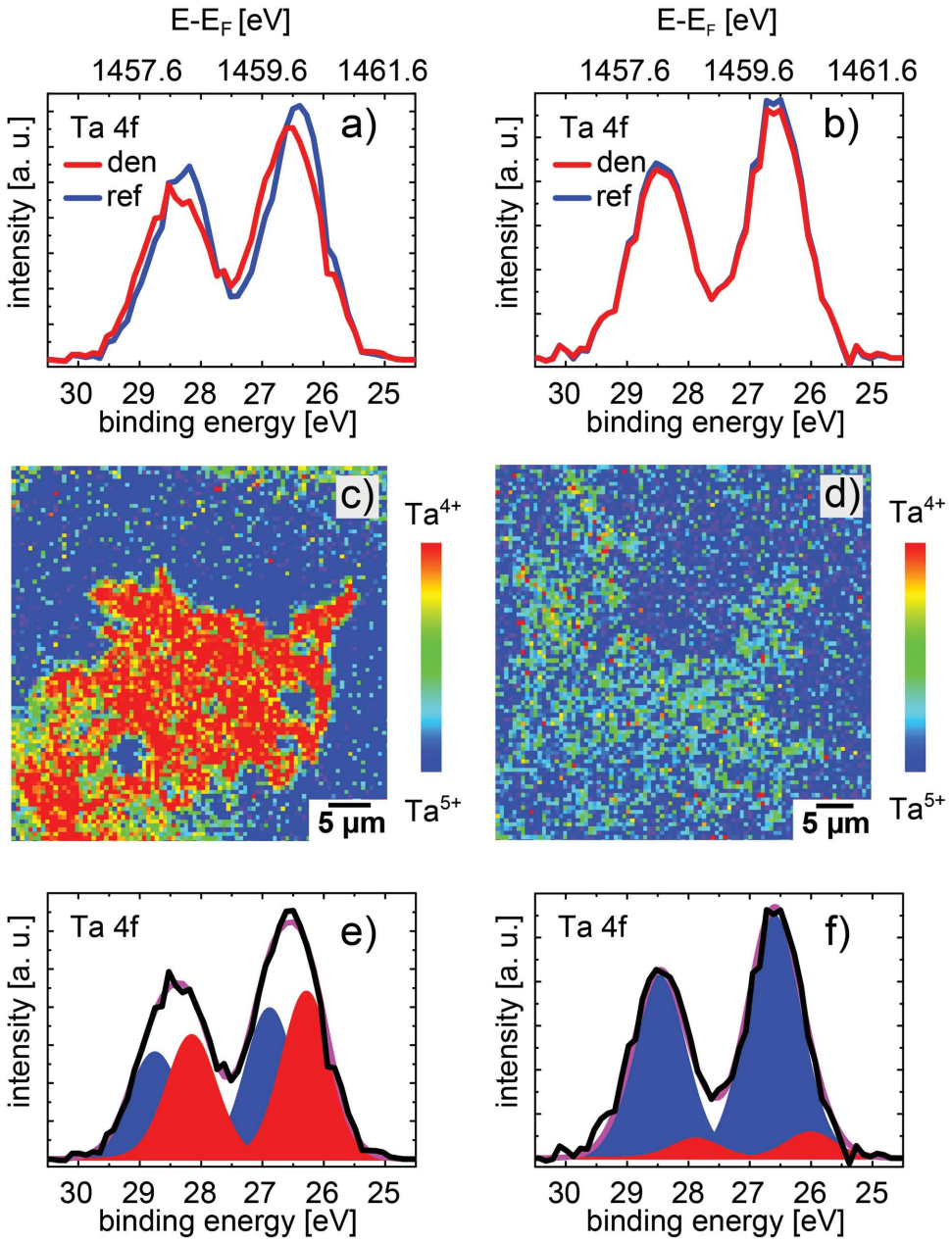


**Figure 5.** PEEM analysis of $Ta_2O_{5-x}$ devices. Extracted Ta 4f core level spectra from the dendrite-like structure (red curve) and the reference region (blue curve) for a) LRS and b) HRS cell. False color maps showing the distribution of $Ta^{4+}$ (yellow) and $Ta^{5+}$ (blue) for c) the LRS and d) HRS. Ta 4f XPS spectra extracted from the dendrite-like region for e) LRS and f) HRS cell. The spectra were fitted with two components, one for $Ta_2O_{5-x}$ (blue) and one for the low binding energy component $TaO_2$ (red), the total fit is presented by the pink curve.

from the threshold spectra, the Ta 4f spectra of the dendrite-like region for the LRS cell is shifted toward higher binding energies (lower electron kinetic energies) compared to the unaltered surrounding. We compare the core level positions of the $Ta_2O_5$ component for the reference and the dendrite-like structure. The components are shifted 0.4 and 0.1 eV toward higher binding energies for LRS and HRS, respectively. These values are in excellent agreement with the results of the work function scans. Therefore, we can exclude that the relative shifts of the work function are induced by a change in the surface dipole. In consequence, we conclude that the conduction band edge is closer to the electrochemical potential, which is consistent with LC-AFM measurements.

Closer inspection of the extracted spectra leads to the impression that for the LRS cell, the dendrite-like region has a broader peak shape than the unaltered surrounding. The drop between the two core levels is less pronounced. For the HRS cell the spectra of the dendrite-like region and the unaltered surrounding have a nearly identical peak shape. This indicates that an additional component must be present in the dendrite-like region for the LRS cell. For quantification, the spatially resolved Ta 4f core level scans for both cells were analyzed

by principal components analysis (PCA), which is a common procedure for noise reduction and the handling of large data sets such as spatially resolved spectroscopy.[38,39] For each pixel the spectrum was fitted with a peak model developed for the spectra shown in Figure 5 a, which consists of two different oxide components to account for the broadened peak shape. One component represents the $Ta_2O_5$ and the other one the reduced species $TaO_2$, which has a shift of 0.6 eV toward lower binding energies compared to $Ta_2O_5$. This is in good agreement with values published in literature[40–42] and the choice of these components for the fitting routine is justified from the quality of the fits shown in Figure 5e,f.

The spatial distribution of the $Ta^{4+}$ component is displayed in Figure 5c,d as false color maps for the LRS and HRS cells, respectively. The red regions correspond to an increased concentration of $Ta^{4+}$, while the blue region indicates the absence of a reduced tantalum component. For both cells, the chemical composition of the dendrite-like region is rather homogeneous, with a strong $Ta^{4+}$ contribution for the LRS cell and only a very weak $Ta^{4+}$ contribution for the HRS cell. This is also clearly visible in the fitted core level spectra of the dendrite-like region, displayed in Figure 5e,f. The $TaO_2$ component (red) is strongly increased in the case of the LRS, whereas this component is decreased for the HRS. Therefore, we conclude that during switching between LRS and HRS the entire former $Pt/Ta_2O_{5-x}$ interface of the dendrite-like region changes the valence state (cf. false color maps Figure 5c,d).

## 3. Discussion

Microscopic measurements and structural analysis show the development of a dendrite-like structure at the former $Pt/Ta_2O_{5-x}$ interface during the electroforming with a positive voltage at the top electrode, whereas for the opposite forming polarity no morphological changes occur. The most likely explanation for this is that the excorporation of oxygen after negative forming does not take place at the upper interface, but at the bottom interface. During the forming process, the tantalum bottom electrode is oxidized and oxygen vacancies are created within the oxide layer. For the positive polarity, on the other hand, oxygen is excorporated at the top interface.

As discussed in the introduction, such forming steps in memristive devices are commonly attributed to an enhanced oxygen diffusion due to Joule heating within a small filament. The nanodiffraction measurements performed on our cells, however, show that the amorphous $Ta_2O_{5-x}$ did not crystallize during the electroforming. For the crystallization by post-deposition annealing of thin amorphous $Ta_2O_{5-x}$ films a temperature above 600 °C [43,44] was reported in literature. Therefore, we assume that the temperature reached during the electroforming process is below or equal to 600 °C. To substantiate this assumption, we simulated the temperature development during the formation of a conductive filament caused by electric field and Joule heating with an axial symmetrical model (cf. Figure S3a, Supporting Information). The dendrite-like structures typically have a size of several micrometers and the central part with circular fronts has a diameter of approximately 300 nm. As can be seen in Figure S3b of the Supporting Information the maximum temperature within the simulated model is less than or equal to 900 K for 100 nm sized filaments and the temperature rapidly decreases with increasing radius of the filament. Therefore, it is unlikely that an electric field and Joule heating as reported in literature [11,18,20] result in these spacious dendrite-like structures. Nevertheless, changes in the tantalum oxygen bonds are observed in amorphous materials for annealing at lower temperatures,[45] which is in good agreement with the observation of a new amorphous, conducting phase in the dendrite-like region.[22,23]

Instead of oxygen diffusion due to Joule heating within a small filament, the properties of the $Pt/Ta_2O_{5-x}$ interface appear to affect the electrical forming process, since the dendrite-like structures occur only at one polarity. In fact, MIM structures with a sputtered platinum electrode (same layer structure as the evaporated ones described above) exhibit smaller morphological changes after electroforming with positive voltage at the top electrode (cf. **Figure 6**a). The forming voltage of these cells (6.0 V) is lower than in those with evaporated top electrodes (7.6 V) (for detail see Supporting Information, Figure S4). One possible explanation for this preparation-method-dependent forming behavior is an additional adsorbate layer at the evaporated $Pt/Ta_2O_{5-x}$ interface, containing water or hydrocarbons, which introduce an additional capacitance to the layer stack that raises the forming voltage. In the Supporting Information we demonstrate by XPS that the adsorbate layer caused by the ex situ preparation of the top electrode is still present after the evaporation of platinum (cf. Figure S5, Supporting Information). This interfacial layer should be smaller or even absent for the sputtered electrodes due to argon bombardment of the $Ta_2O_{5-x}$ surface during sputter deposition. A strong impact of the Pt deposition method on the switching performance has been previously observed for Nb doped $SrTiO_3$ single crystals devices and attributed to the presence of adsorbate layers.[46]

The development of structures with a similar shape as the dendrite-like structure observed here for the evaporated

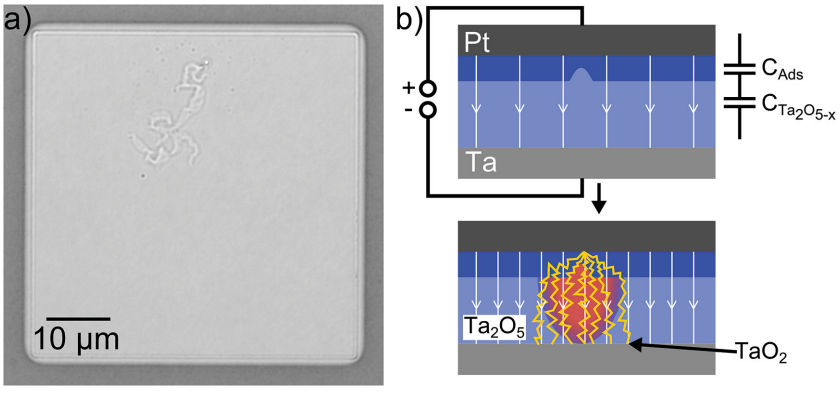


**Figure 6.** a) Microscope image of a $Pt/Ta_2O_{5-x}/Ta$ structure with a sputter-deposited top electrode after electroforming. b) Scheme of the MIM structure with an adsorbate layer in between the $Pt/Ta_2O_{5-x}$ interface. The avalanche discharge preferentially takes place at the impurities.

Pt electrodes was reported after an electrical breakdown during a $Ta_2O_{5-x}$ anodization process in aqueous electrolytes,[47,48] where microfissures or cracks occurred. Most of the reports describe this breakdown process with a model based on the avalanche mechanism.[49,50] At the metal oxide/electrolyte interface, electrons are injected and accelerated by a high electric field on the order of MV/cm. The injected electrons collide with ions in the metal oxide and generate new electrons, which are also accelerated in the high electric field. This process is a chain reaction of electron generation. Consequently, an electron avalanche is initialized, which leads to an electrical breakdown after a critical current is reached. During this process sparking and scintillation were observed at the electrolyte/oxide interface, where the discharge paths develop orthogonal to the electric field.[49,51]

This interface-dominated electrical breakdown with similar dendritic structures can also explain the electroforming process in our MIM structures with adsorbate layers. We assume that at the beginning of the forming process the electric field is homogeneously distributed over the MIM structures (Figure 6b). The applied voltages drop across the adsorbate layer and the $Ta_2O_{5-x}$ layer. At a certain voltage, an electron avalanche discharge appears in the interface layer between Pt and $Ta_2O_{5-x}$. These discharges evolve orthogonal to the applied electric field and lead to the dendrite-like structure in the $Ta_2O_{5-x}$. The induced local heat and the high electric field lead to a reduction of the $Ta_2O_{5-x}$ layer over the whole dendrite-like structure and the entire layer thickness since the device is transformed to the On-state after the forming procedure. We estimate the response time for the current compliance to 1 µs. This leads to a current overshoot in the device, which was previously attributed to parasitic capacitances.[52,53] The discharge is propagated laterally over the device, but the current compliance limits only the current between top and bottom electrode. Therefore, the current overshoot in cells with a pronounced interface adsorbate layer is larger than in those without an adsorbate layer, because the current compliance limits the current in the devices after the local soft-breakdown due to the avalanche discharge.

The circular central part of the dendrite-like structure, which we assume to be the point where the electron avalanche was initiated, appears to be randomly distributed over the entire electrode interface. This indicates that the discharges preferably occur at impurities or pre-existing defects due to field enhancement or elevated positions at these points (Figure 6b). In the Supporting Information single frames of a movie show the time development of the dendrite-like structure (cf. Figure S6, Supporting Information), which support the assumption about the lateral propagation of the structure from single points. In **Figure 7**a the evolution process of the dendrite-like structure is schematically illustrated, where the dendrite-like structure arises at a starting point and develops perpendicular to the electric field.

From the PEEM results, the reduced phase emerging in the dendrite-like structure during this discharge can be assigned to $TaO_2$, which is a conductive phase.[14] The LC-AFM measurements support this observation and show that the dendrite-like structure is reduced over the entire layer thickness. After the development of the dendrite-like structures, the cells can be switched between HRS and LRS. The presented

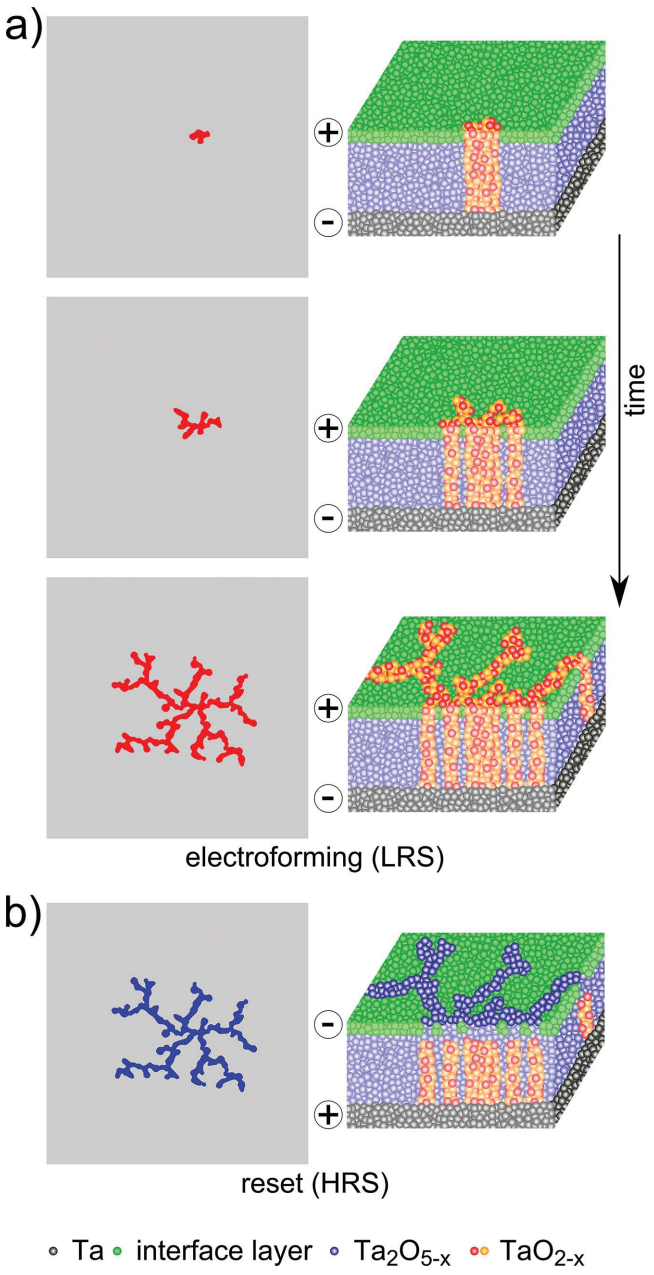


**Figure 7.** a) Illustration of the evolution of the dendrite-like structure at the top electrode during electroforming with a positive bias. (The aspect ratios of the image are not drawn to scale.) The structure starts to grow at an initial point and develops perpendicular to the applied electrical field. Schematic profile of the dendrite-like structure beneath platinum top electrode with an interfacial layer (consisting of $H_2O$ and hydrocarbons) (green circles), $Ta_2O_{5-x}$ (blue circles), Ta bottom electrode (gray circles), and the conductive path (orange/yellow circles) developed after forming with a positive voltage at the platinum top electrode. Additional information is available in the Supporting Information (cf. Figure S6, Supporting Information). b) During reset, the reduced region is oxidized leading to a valence change between $Ta^{4+}$ and $Ta^{5+}$. The insulating gap (a surface layer of fully oxidized $Ta_2O_5$) arising after reset was estimated to be larger or equal to 2.5 nm.

spectromicroscopic results show that during switching between LRS and HRS the concentration of $TaO_2$ within the dendrite-like structure is decreased, caused by a reoxidation of $Ta^{4+}$ to

$Ta^{5+}$. Therefore, we assume that the oxygen vacancies are pushed downward by an electric field to the bottom electrode. At the top interface, an insulating gap (a surface layer of fully reoxidized $Ta_2O_5$) arises over the entire former $Pt/Ta_2O_{5-x}$ interface of the dendrite-like structure, which leads to a resistance of several MΩ in the MIM structure. As the inelastic mean free path for photoelectrons at a kinetic energy of 1460 eV is approximately 2.3 nm,[54] we estimate that this insulating gap between the top electrode and the conductive region is greater than or equal to approximately 2.5 nm. A side view of the conductive path for the different resistance states is depicted in Figure 7b.

This is an explicit proof of the valence change mechanism in a $Ta_2O_{5-x}$ MIM structure, where we can correlate the occurrence or the absence of enhanced conductivity in the dendrite-like structure with the reduction to $TaO_2$ or the re-oxidation to $Ta_2O_{5-x}$, respectively. In comparison to observations of filamentary switching in previous reports,[14,22,23] the reduction and reoxidation takes place not within a small area of a few 100 nm, but over the entire former $Pt/Ta_2O_{5-x}$ interface of the dendrite-like region with a size of several micrometers, which is a consequence of the preparation-induced pronounced interface adsorbate layer.

## 4. Conclusion

We have experimentally examined the former $Pt/Ta_2O_{5-x}$ interface of $Pt/Ta_2O_{5-x}/Ta$ devices after switching and in situ mechanical removal of the top electrode. Only for positive bias at the former $Pt/Ta_2O_{5-x}$ interface a dendrite-like structure arises due to an additional capacitance at the interface, which is caused by an interfacial adsorbate layer (containing water or hydrocarbons). As a result of the avalanche discharge within the adsorbate layer, heat is induced to the $Ta_2O_{5-x}$ leading to the reduction of the entire dendrite-like structure. During subsequent switching between HRS and LRS, a valence change between $Ta^{5+}$ and $Ta^{4+}$ takes place within the entire former $Pt/Ta_2O_{5-x}$ interface of dendrite-like structure. It is important to note that in case of an avalanche discharge in the adsorbate layer, the propagation of the dendrite-like structure and the resulting area where a valence change takes place during switching cannot be controlled by the current compliance. Therefore, under these circumstances, no direct correlation between filament diameter and current compliance can be expected, as reported in the literature.[55,56]

Since $Ta_2O_{5-x}$ is one of the most promising candidates considered for future memristive cells, these results are essential for the further understanding and improvement of this important class of future nanoelectronics devices, especially regarding the impact of the metal/metal oxide interfacial properties.

## 5. Experimental Section

The MIM structures were prepared by DC sputtering on a silicon substrate covered with 430 nm thermal silicon oxide. A 50 nm thick tantalum film was deposited from a metallic target with a power of 30 W in pure argon under high pressures ($7 \times 10^{-3}$ mbar). Afterward, a 15 nm $Ta_2O_{5-x}$ thick film was sputter-deposited in situ at $3.5 \times 10^{-2}$ mbar by reactive DC sputtering in a 75% Ar and 25% $O_2$ atmosphere with a power of 20 W. The top electrodes with a size of 50 × 50 µm were structured by ex situ deposition of 70 nm Pt on top of the $Ta_2O_{5-x}$ by electron beam evaporation through a shadow mask. The sputter-deposited Pt electrodes were prepared ex situ by DC sputtering with a power of 30 W in pure argon with a pressure of $7 \times 10^{-3}$ mbar.

For electrical characterization, the top electrode was contacted with tungsten whisker probes. The bottom electrode was contacted by wire bonding with an Al wire. After the forming process some of the cells were kept in the LRS and others were switched back into HRS for subsequent spectromicroscopic analysis.

The top electrode was delaminated with an adhesive copper tape after evaporation of a homogeneous 70 nm thick Pt layer onto the entire sample. For the PEEM measurements, the delamination of the Pt electrodes and the transfer to the PEEM carried out under UHV conditions.

The SEM measurements were performed with a Hitachi SU 8000 field-emission microscope.

The topography measurements were conducted with a Cypher Atomic Force Microscope from Asylum Research operated in tapping mode.

The combined AFM/LC-AFM measurements were performed using an Omicron VT-SPM system operating at room temperature under UHV conditions. The detection of the local surface conductance was achieved by the use of silicon cantilevers with a boron doped polycrystalline diamond coating. The cantilever tips had a nominal radius of less than 10 nm and a spring constant of 25 N $m^{-1}$ (AppNano, DD-ACTA-10). Applying gap voltages of up to 10 V between the tip and the sample induced a maximum current flow of ≈30 nA. The force setpoint was limited to 2 nN in order to minimize a possible effect of the contact mode measurements on the surface morphology.

TEM specimens were cut using focused ion beam milling with a Ga ion beam at 30 kV beam energy and finally polished at 5 kV on a FEI Helios NanoLab 400S workstation. TIA (TEM imaging & analysis) software from FEI was used for the imaging and the analysis.

Nanodiffraction in STEM was performed on a FEI Titan STEM 80–300. The STEM was used in microprobe mode at 300 keV to form a coherent and almost parallel electron probe of around 2 nm. The diffraction patterns were energy filtered with a slit width of 20 eV and recorded by a Gatan 2k slow scan charged coupled device camera system.

PEEM was performed with a NanoESCA from Omicron NanoTechnology GmbH.[57] (pass energy 100 eV; entrance slit 1 mm; energy resolution 400 meV). The electrons for the core level photoelectron spectroscopy measurements were excited with a monochromatic focused X-ray source (Al $K_\alpha$ source, 1486.6 eV). For threshold photoemission, a mercury lamp was used. Various series of images were taken at increasing electron kinetic energies with a step size of 0.1 eV. Threshold and core level photoemission spectra were extracted from the resulting image stack in different regions of interest. The image stacks were analyzed and spectra were extracted using the IGOR Pro Software. The fitting of the core level photoelectron spectra and the principal component analysis were performed with CasaXPS Version 2.3.16 after binning of 4 × 4 px for better statistics.

XPS measurements were performed on a PHI-5000 versa-probe II with a monochromatic Al $K_\alpha$ source (1486.6 eV) using a detection angle of 45°.

## Supporting Information

Supporting Information is available from the Wiley Online Library or from the author.

## Acknowledgements

This work was in part funded by the Deutsche Forschungsgemeinschaft (DFG) within the SFB 917. K.S. was supported by the Initiative and Networking Fund of the German Helmholtz Association, Helmholtz Virtual

Institute VH-VI-442 MEMRIOX. C.B. and R.D. also acknowledge funding from the W2/W3 program of the Helmholtz association. The authors would like to thank Max Kruth for the preparation of the TEM lamella.

Received: July 7, 2015
Revised: September 10, 2015
Published online: October 30, 2015

[1] R. Waser, M. Aono, *Nat. Mater.* **2007**, *6*, 833.
[2] A. Sawa, *Mater. Today* **2008**, *11*, 28.
[3] R. Waser, R. Dittmann, G. Staikov, K. Szot, *Adv. Mater.* **2009**, *21*, 2632.
[4] J. J. Yang, M. D. Pickett, X. Li, D. A. A. Ohlberg, D. R. Stewart, R. S. Williams, *Nat. Nanotechnol.* **2008**, *3*, 429.
[5] P. Gonon, M. Mougenot, C. Vallee, C. Jorel, V. Jousseaume, H. Grampeix, F. El Kamel, *J. Appl. Phys.* **2010**, *107*, 74507/1.
[6] J. P. Strachan, J. J. Yang, L. A. Montoro, C. A. Ospina, A. J. Ramirez, A. L. D. Kilcoyne, G. Medeiros-Ribeiro, R. S. Williams, *Beilstein J. Nanotechnol.* **2013**, *4*, 467.
[7] S. Kim, S. Choi, J. Lee, W. D. Lu, *ACS Nano* **2014**, *8*, 10262.
[8] R. Muenstermann, T. Menke, R. Dittmann, S. Mi, C.-L. Jia, D. Park, J. Mayer, *J. Appl. Phys.* **2010**, *108*, 124504/1.
[9] M. Janousch, G. I. Meijer, U. Staub, B. Delley, S. F. Karg, B. P. Andreasson, *Adv. Mater.* **2006**, *19*, 2232.
[10] C. Moreno, C. Munuera, S. Valencia, F. Kronast, X. Obradors, C. Ocal, *Nano Lett.* **2010**, *10*, 3828.
[11] Y. B. Nian, J. Strozier, N. J. Wu, X. Chen, A. Ignatiev, *Phys. Rev. Lett.* **2007**, *98*, 146403/1.
[12] S. Kim, S. Choi, W. Lu, *ACS Nano* **2014**, *8*, 2369.
[13] F. Miao, W. Yi, I. Goldfarb, J. J. Yang, M. X. Zhang, M. D. Pickett, J. P. Strachan, G. Medeiros-Ribeiro, R. S. Williams, *ACS Nano* **2012**, *6*, 2312.
[14] G.-S. Park, Y.-B. Kim, S. Y. Park, X. S. Li, S. Heo, M. J. Lee, M. Chang, J. H. Kwon, M. Kim, U.-I. Chung, R. Dittmann, R. Waser, K. Kim, *Nat. Commun.* **2013**, *4*, 2382/1.
[15] J. P. Strachan, M. D. Pickett, J. J. Yang, S. Aloni, A. L. D. Kilcoyne, G. Medeiros-Ribeiro, R. S. Williams, *Adv. Mater.* **2010**, *22*, 3573.
[16] J. P. Strachan, J. J. Yang, R. Muenstermann, A. Scholl, G. Medeiros-Ribeiro, D. R. Stewart, R. S. Williams, *Nanotechnology* **2009**, *20*, 485701.
[17] D.-H. Kwon, K. M. Kim, J. H. Jang, J. M. Jeon, M. H. Lee, G. H. Kim, X.-S. Li, G.-S. Park, B. Lee, S. Han, M. Kim, C. S. Hwang, *Nat. Nanotechnol.* **2010**, *5*, 148.
[18] K. Szot, W. Speier, G. Bihlmayer, R. Waser, *Nat. Mater.* **2006**, *5*, 312.
[19] Ch. Lenser, Z. Connell, A. Kovacs, R. Dunin-Borkowski, A. Koehl, R. Waser, R. Dittmann, *Appl. Phys. Lett.* **2013**, *102*, 183504.
[20] A. Sharma, M. Noman, M. Abdelmoula, M. Skowronski, J. Bain, *Adv. Funct. Mater.* **2014**, *24*, 5522.
[21] Z. Wei, Y. Kanzawa, K. Arita, Y. Katoh, K. Kawai, S. Muraoka, S. Mitani, S. Fujii, K. Katayama, M. Iijima, T. Mikawa, T. Ninomiya, R. Miyanaga, Y. Kawashima, K. Tsuji, A. Himeno, T. Okada, R. Azuma, K. Shimakawa, H. Sugaya, T. Takagi, R. Yasuhara, H. Horiba, H. Kumigashira, M. Oshima, in *IEEE Int. Electron Devices Meeting* **2008**, IEEE, Piscataway, NJ, USA **2008**, pp. 1–7.
[22] J. P. Strachan, G. Medeiros-Ribeiro, J. J. Yang, M.-X. Zhang, F. Miao, I. Goldfarb, M. Holt, V. Rose, R. S. Williams, *Appl. Phys. Lett.* **2011**, *98*, 242114.
[23] F. Miao, J. P. Strachan, J. J. Yang, M.-X. Zhang, I. Goldfarb, A. C. Torrezan, P. Eschbach, R. D. Kelly, G. Medeiros-Ribeiro, R. S. Williams, *Adv. Mater.* **2011**, *23*, 5633.
[24] Y. Yang, S. Choi, W. Lu, *Nano Lett.* **2013**, *13*, 2908.
[25] S. Schmelzer, E. Linn, U. Böttger, R. Waser, *IEEE Electron Device Lett.* **2013**, *34*, 114.
[26] S. C. Na, J. J. Kim, M. C. Chun, D. H. Jin, S. E. Ahn, B. S. Kang, *Appl. Phys. Lett.* **2014**, *104*, 123503/1.
[27] V. I. Gibalov, G. J. Pietsch, *Plasma Sources Sci. Technol.* **2012**, *21*, 024010.
[28] J. Cazaux, *Ultramicroscopy* **2010**, *110*, 242.
[29] O. Renault, R. Brochier, A. Roule, P.-H. Haumesser, B. Bromker, D. Funnemann, *Surf. Interface Anal.* **2006**, *38*, 375.
[30] K. Tsukada, H. Inoue, F. Katayma, K. Sakai, T. Kiwa, *Jpn. J. Appl. Phys.* **2012**, *51*, 015701.
[31] B. Xiao, S. Watanabe, *Nanoscale* **2014**, *6*, 10169.
[32] R. J. Bondi, M. P. Desjarlais, A. P. Thompson, G. L. Brennecka, M. J. Marinella, *J. Appl. Phys.* **2013**, *114*, 203701.
[33] K. Wandelt, *Appl. Surf. Sci.* **1997**, *111*, 1.
[34] N. D. Lang, W. Kohn, *Phys. Rev. B* **1970**, *1*, 4555.
[35] L. Diederich, O. M. Küttel, P. Aebi, L. Schlapbach, *Surf. Sci.* **1998**, *418*, 219.
[36] W. Li, D. Y. Li, *J. Chem. Phys.* **2005**, *122*, 064708.
[37] M. T. Greiner, L. Chai, M. G. Helander, W. M. Tang, Z. H. Lu, *Adv. Funct. Mater.* **2012**, *22*, 4557.
[38] H. Kim, O. Renault, A. Tyurnina, J.-P. Simonato, D. Rouchon, D. Mariolle, N. Chevalier, J. Dijon, *Appl. Phys. Lett.* **2014**, *105*, 011605.
[39] J. Walton, N. Fairley, *J. Electron Spectrosc. Relat. Phenom.* **2005**, *148*, 29.
[40] O. Kerrec, D. Devilliers, H. Groult, P. Marcus, *Mater. Sci. Eng., B* **1998**, *55*, 134.
[41] B. Diaz, J. Swiatowska, V. Maurice, A. Seyeux, E. Härkönen, M. Ritala, S. Tervakangas, J. Kolehmainen, P. Marcus, *Electrochim. Acta* **2013**, *90*, 232.
[42] B. Diaz, J. Swiatowska, V. Maurice, M. Pisarek, A. Seyeux, S. Zanna, S. Tervakangas, J. Kolehmainen, P. Marcus, *Surf. Coat. Technol.* **2012**, *206*, 3903.
[43] G. S. Oehrlein, F. M. d'Heurle, A. Reisman, *J. Appl. Phys.* **1984**, *55*, 3715.
[44] E. Atanassova, N. Novkovski, A. Paskaleva, M. Pecovska-Gjorgjevich, *Solid State Electron.* **2002**, *46*, 1887.
[45] H. Ono, K.-I. Koyanagi, *Appl. Phys. Lett.* **2000**, *77*, 1431.
[46] E. Mikheev, B. D. Hoskins, D. B. Strukov, S. Stemmer, *Nat. Commun.* **2014**, *5*, 3990.
[47] J. M. Albella, I. Montero, M. Fernández, J. M. Martìnez-Duart, *J. Appl. Electrochem.* **1981**, *11*, 525.
[48] L. Vázquez, I. Montero, J. M. Albella, *Chem. Mater.* **1995**, *7*, 1680.
[49] V. Kadary, N. Klein, *J. Electrochem. Soc.* **1980**, *127*, 139.
[50] J. M. Albella, I. Montero, J. M. Martínez-Duart, *J. Mater. Sci.* **1991**, *26*, 3422.
[51] K. C. Kalra, P. Katayal, K. C. Singh, *Thin Solid Films* **1989**, *177*, 35.
[52] H. J. Wan, P. Zhou, L. Ye, Y. Y. Lin, T. A. Tang, H. M. Wu, M. H. Chi, *IEEE Electron Device Lett.* **2010**, *31*, 246.
[53] S. Tirano, L. Perniola, J. Buckley, J. Cluzel, V. Jousseaume, C. Muller, D. Deleruyelle, B. De Salvo, G. Reimbold, *Microelectron. Eng.* **2011**, *88*, 1129.
[54] C. J. Powell, A. Jablonski, *NIST Electron Inelastic-Mean-Free-Path Database-Version 1.2*, National Institute of Standards and Technology, Gaithersburg, MD, USA **2010**.
[55] D. Ielmini, F. Nardi, C. Cagli, *Nanotechnology* **2011**, *22*, 254022/1.
[56] U. Celano, L. Goux, A. Belmonte, K. Opsomer, A. Franquet, A. Schulze, C. Detavernier, O. Richard, H. Bender, M. Jurczak, W. Vandervorst, *Nano Lett.* **2014**, *14*, 2401.
[57] M. Escher, N. Weber, M. Merkel, C. Ziethen, P. Bernhard, G. Schönhense, S. Schmidt, F. Forster, F. Reinert, B. Krömker, D. Funnemann, *J. Phys. Condens. Mater.* **2005**, *17*, S1329.